Journal of MATERIALS RESEARCH

Article
DOI:10.1557/s43578-021-00394-0

MSELD $SnS_{1-x}Se_x$ alloy thin films towards efficient structural and bandgap engineering for photonic devices

Arun Banotra[1,a], Naresh Padha[1]

[1] Department of Physics, University of Jammu, Jammu 180006, India
[a] Address all correspondence to this author. e-mail: arunbanotra451@gmail.com

Received: 6 March 2021; accepted: 14 September 2021; published online: 20 September 2021

Ternary $SnS_{1-x}Se_x$ alloy thin films prepared by depositing stacks of varied elemental weight percentages using multisource sequential elemental layer deposition (MSELD) technique. The focus of investigation is to achieve $SnS_{1-x}Se_x$ phase by varying 'Se' constituent in the film for large scale photovoltaic (PV) devices. The substitution of varied 'Se' weight percentages leads to the formation of ternary $SnS_{1-x}Se_x$ phases along with the presence of changed polytypic Sn_xS_y phases causing structural deformations. These structural deformations leads to variation in unit cell volume and axis strain due to insertion of higher atomic radii of selenium ('Se') in place of Sulphur ('S'). This structural engineering results into variation of direct–indirect bandgaps, higher absorption and excellent electrical properties viz. resistivity (4.5–66.9 Ωcm), mobility (1.8–9.8 cm^2/Vs) and carrier concentration (~ 10^{16} to 10^{17} cm^{-3}) for their use as photosensitive layer in the development of large scale photonic devices.

Introduction

Recently inorganic materials attracted attention as effective photovoltaic absorbers in the visible–NIR region due to their long carrier diffusion length, tunable direct bandgap, weak exciton binding energy and high defect tolerance. These merits display superior performance to raise photo conversion and to achieve higher solar cell performance. Thus, exploration of cost effective, less toxic and earth abundant materials for their use in photovoltaic absorbers seems interesting area of research [1]. These photovoltaic absorbers are considered as an alternate renewable energy source which leads to the generation of power at the terawatt level with sustainable future development. This goal of low cost, less toxic and higher power generation cannot be achieved with the already developed technologies of CdTe, Si and CIGS material due to the presence of toxic constituents along with issue in their disposal management and indirect bandgap (Si) [2–5]. Thus, attempts were made to develop alternate photovoltaic absorbers for efficient energy conversion to achieve facile methodology for large scale production. This objective is possible by using low cost, less toxic and earth abundant materials like Cu, Zn, Sn and S for the development of CZTS materials. Recent research investigations in CZTS materials reveal excellent properties as high absorption ~ 10^4 cm^{-1}, direct bandgap of 1.5 eV and enhanced solar photo conversion efficiency (~ 11.20%) [6–9]. According to the literature reports, the performance of solar cell is highly sensitive to structure and composition which can be enhanced by offering suitable modifications. These modifications were often seen due to the presence of various binary and ternary impurity phases in CZTS materials and lead to demonstrate deviations in their characteristics. Thus, efficient CZTS solar cells can be realized by controlling physical properties of their binary and ternary derivatives. The motivational aspect behind the use of these material is their achievable (Shockley Quiesser) efficiency limit > 30%. The sulphide based CZTS solar cells shows an efficiency of 11.20% which is very low as compared to the SQ limit of 31.5% [10]. However, selenide based CZTS solar cells showed a practical efficiency of 9.15% with SQ limit of 30.9%. Besides this, the SQ efficiency even with losses is 27% and 26% for sulphide and selenide based CZTS solar cells, respectively. Upto now, the CZTS material capabilities are not explored efficiently. However, a record efficiency of 12.6% for CZTSSe solar cells observed irrespective of their SQ limit of 32.8% [11–13]. Hence, sulpho-selenide based solar cells exhibit higher efficiency apart from its binary counterparts like SnS (4.36% [14]) and SnSe (1.40%) which presents practically lower solar efficiency. Thus, emphasis must be made for the development of these sulpho-selenide based absorbers with enhanced physical characteristics for efficient photo conversion. These

© The Author(s), under exclusive licence to The Materials Research Society 2021

IV-VI chalcogenide based solar cells has recently attracted great attention and can achieve bandgap tailoring by the incorporation of 'S' or 'Se' in SnSe and SnS material systems, respectively. Recent reports reveals material properties can also be enhanced by forming solid solutions (alloying) in optimizing material characteristics through elemental doping and band convergence. Alloying of materials allow engineering of bands in terms of their shape, gap and positions corresponding to their changed effective mass, bipolar effect and band alignment and thus, leads to yield high performance material characteristics for their use as photovoltaic, photodetectors, photoelectrochemical sensors, EM tuners and thermoelectric devices [15, 16]. One of the major advantage to undertake alloying (solid solutions) of $SnS_{1-x}Se_x$ compound semiconductors is their wider solar selective spectral response with capacity to engineer optical bandgap from 1.3 eV (950 nm) to 0.8 eV (1550 nm) in the NIR region of the EM spectrum [17]. Few reports on the formation of $SnS_{1-x}Se_x$ based solar cell demonstrate maximum lab efficiency of 1.15% deposited using chemical bath deposition [18].

Previously, $SnS_{1-x}Se_x$ phase grown in the form of single crystals using melt quenching [19] and direct vapour transport [20] while thin film formation has been achieved using electrodeposition [21], chemical bath deposition [22], screen printing [23], thermal evaporation [24], electrochemical deposition [25] and co-evaporation [26]. Besides this, $SnS_{1-x}Se_x$ has also been grown in the form of nanocrystals [17, 27], nanosheets [28], solid solution, ultrathin/circular nanosheets [29, 30] using pulsed layer deposition [27], hydrothermal chemical exfoliation [31], cluster expansion and Physical vapour deposition [29, 30], respectively.

In recent past, the main challenges in PV technology are scaling up of high device efficiency at industrial scale using lab techniques. This gap between lab scale techniques and commercially available solar modules is usually restricted by the presence of inhomogenieties in the cell layer during deposition at industrial scale. To maintain lab efficiency at industrial scale homogeneous film deposition over the large area is required. These large scale depositions can be achieved by depositing solar cell structures using vacuum deposition processes like sputtering thermal and co-evaporation [32–34]. Recently, exploration to achieve large scale thin film production by standardization of thermal evaporation using multisource sequential elemental layer deposition and similar techniques like sulphurization and selenization have already been initiated [35–43]. Present investigation demonstrate the use of facile MSELD deposition technique for the development of $SnS_{1-x}Se_x$ alloy thin films for implementing future innovative photonic structures for low cost high performance PV devices.

To achieve the desired phase formation, Post deposition treatments (PDTs) becomes an effective technique for the development of efficient chalcogenide material based solar cells. The PDTs in 'S' and 'Se' atmosphere reported to be undertaken by researchers to develop SnS and SnSe based solar cells have achieved solar cell efficiency of 2.63% and 1.4%, respectively [40, 44]. Besides this, PDTs in 'S' and 'Se' atmosphere exhibits excessive loss of constituents in maintaining these atmospheres during the whole annealing process. Keeping into consideration, the loss of constituents, the sulphurization and selenization technique in the present investigation has been used in a modified way to achieve homogeneous ternary $SnS_{1-x}Se_x$ alloy phase thin films for solar application.

In the present methadology, Sn, S, and Se constituents of varied weight percentages were deposited using MSELD technique to achieve $SnS_{1-x}Se_x$ alloy based ternary thin films. Post deposition annealing allows structural and bandgap engineering on changed film constituents. Such a tuned synthesis of SnS_xSe_{1-x} in the form of alloy exhibits its use as narrow band (1.4–0.8 eV) solar absorbers having absorption in Vis–NIR region and used in high performance photonic applications. Schematic sketch of the deposited MSELD $SnS_{1-x}Se_x$ Stack films with changed composition using thermal evaporator has been shown in Fig. 1.

Results and discussion

Compositional behaviour of post annealed MSELD $SnS_{1-x}Se_x$ stack alloy thin films

The atomic % of the MSEL deposited stacks of varied Sn, S and Se stack layers annealed at 623 K indexed as S1 to S6 and presented in Table 1. The film S1 found to have S/Sn ratio of 1.01 and demonstrate SnS phase formation on annealing at 623 K. This ratio of 1.01 (Sn: S) has been achieved by depositing MSELD layers of 'Sn' and 'S' using weight percentages (Sn: 69.60; S: 30.40) of the constituents. However, deposition of different layer thicknesses of 'Se' on SnS changes film stoichiometry and demonstrates the formation of ternary alloy films indexed from S2 to S5 (Table 1). This alloy phase tuned composition was maintained by depositing the different weight percentages of 'Se' constituents on SnS (Sn: 69.60; S: 30.40). This leads to the formation of ternary alloy as has been confirmed from EDAX in which the changes in 'Se' and 'S' constituents have been observed significantly with changed 'Se' content by varying layer thickness. The increased thickness of 'Se' layer in the films (S2–S5) leads to the formation of $SnS_{0.67}Se_{0.33}$ (S2), $SnS_{0.40}Se_{0.60}$ (S3), $SnS_{0.26}Se_{0.74}$ (S4) and $SnS_{0.13}Se_{0.87}$ (S5) achieved due to solid state reaction kinematics at constant pressure and temperature maintained during deposition and annealing of the stacks. These changes in the alloy formulation with changed thickness of 'Se' layer were corroborated well on the basis of X-ray diffraction, optical, SEM and electrical results. The variation in 'Se' layer constituent exhibit SnS transformation towards SnSe phase through the formation of their ternary and binary polymorphs. The base layer of S2 to

© The Author(s), under exclusive licence to The Materials Research Society 2021

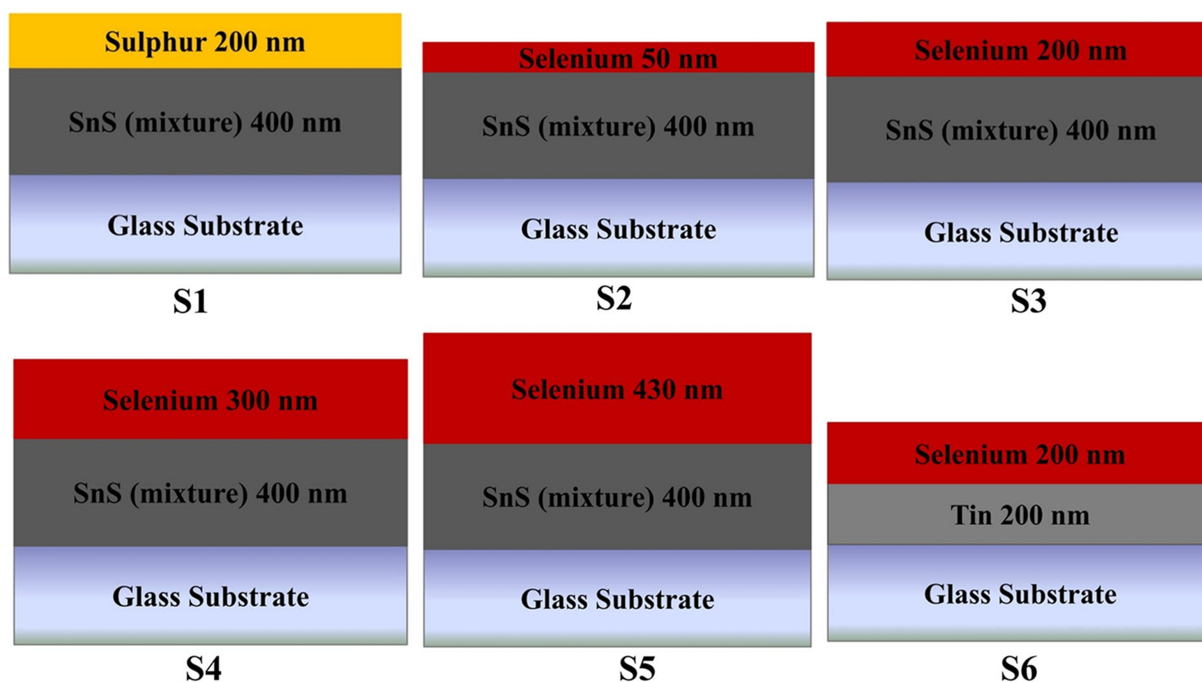

Figure 1: Schematic sketch of the deposited MSELD $SnS_{1-x}Se_x$ Stack films with changed composition using thermal evaporator.

TABLE 1: EDAX data of varied composition of $SnS_{1-x}Se_x$ thin films deposited using MSELD stack.

	Atomic %						
Sample	Sn	S	Se	Se/S + Se	S/S + Se	Sn/Se + S	Compound
S1	50.44	49.56	–	–	–	–	SnS
S2	62.84	24.89	12.27	0.33	0.67	1.69	$SnS_{0.67}Se_{0.33}$
S3	60.05	19.16	27.73	0.59	0.41	1.50	$SnS_{0.40}Se_{0.60}$
S4	53.14	10.19	29.75	0.26	0.74	1.13	$SnS_{0.26}Se_{0.74}$
S5	52.07	6.02	41.91	0.87	0.13	1.08	$SnS_{0.13}Se_{0.87}$
S6	73.13	–	26.87	–	–	–	SnSe

S5 samples were deposited to 400 nm using weight percentages (Sn = 0.79 g, S = 0.21 g) and found to have lower S/Sn ratio from the deposited 1:1 stochiometry. The lower presence of 'S' in the deposited SnS mixture layer (S1) attributed to the incongruent evaporation of the constituent elements due to differences in their vapour pressures and demonstrate predominant 'Sn' phase. The deficit 'S' in the SnS mixture layer is supplemented by depositing varied stoichiometric 'Se' layer to obtain changed $SnS_{1-x}Se_x$ ternary alloy composition films for their suitability in PV devices. These varied stacks (S2 to S5) exhibit major deviations in Sn/(S + Se) ratio on changing the weight percentages of the films (S2 to S5). The films showed decrease in (Sn/S + Se) ratio from 1.69 to 1.08 attributed to the conversion of available 'Sn' material into $SnS_{1-x}Se_x$ phase by increasing 'Se' constituents in the films. The annealing at 623 K showed effective reaction between the constituents (Sn, S & Se) at changed 'Se' concentration. Thus, a technique is demonstrated to achieve ternary $SnS_{1-x}Se_x$ thin films by depositing MSELD stacks of varied composition using facile methadology to achieve PV device technology for large scale development. Apart from these features, present investigation demonstrate an alternative approach to the combination of sulphurization and selenization techniques in a controlled manner to achieve $SnS_{1-x}Se_x$ alloy based thin films. Thus, the present investigation using MSELD demonstrate lower loss of 'Se' to achieve varied composition of constituents as compare to selenization technique. These variations in composition results into structural deformation/transformation with the presence of varied alloyed phases in the form of solid solution and exhibit changed structural, optical and electrical properties for use in photonic device technology. The S2 to S5 stack films results into deeper level diffusion of 'Se' atoms in SnS lattice and transform SnS into $SnS_{1-x}Se_x$ solid solution. However, the film S6 showed higher presence of 'Sn' element as

© The Author(s), under exclusive licence to The Materials Research Society 2021

compared to 'Se' attributed to the deposition of equal weight of 'Sn' and 'Se' using MSELD and their behaviour would be interpreted separately.

Structural behaviour of post annealed MSELD $SnS_{1-x}Se_x$ stack alloy thin films

The structure and cell parameters of the $SnS_{1-x}Se_x$ MSELD stack films of varied composition annealed at 623 K has been examined using GIXRD and presented in Fig. 2a. The change in composition causes variations in the alloy phases and results in deviations in the structural parameter as presented in Table 2. The deposited stack films seems to show smooth surfaces, excellent adhesion with corning glass substrates exhibiting the presence of different mixed binary and ternary phases in the form of sharp polycrystalline peaks. The varied presence of mixed phased binary solid solutions with changed 'Se' concentration represents modifications in the formed SnS lattice. The film S1 ($x=0$) exhibit SnS phase (Sys: Orthorhombic; S. G.: Pnma)

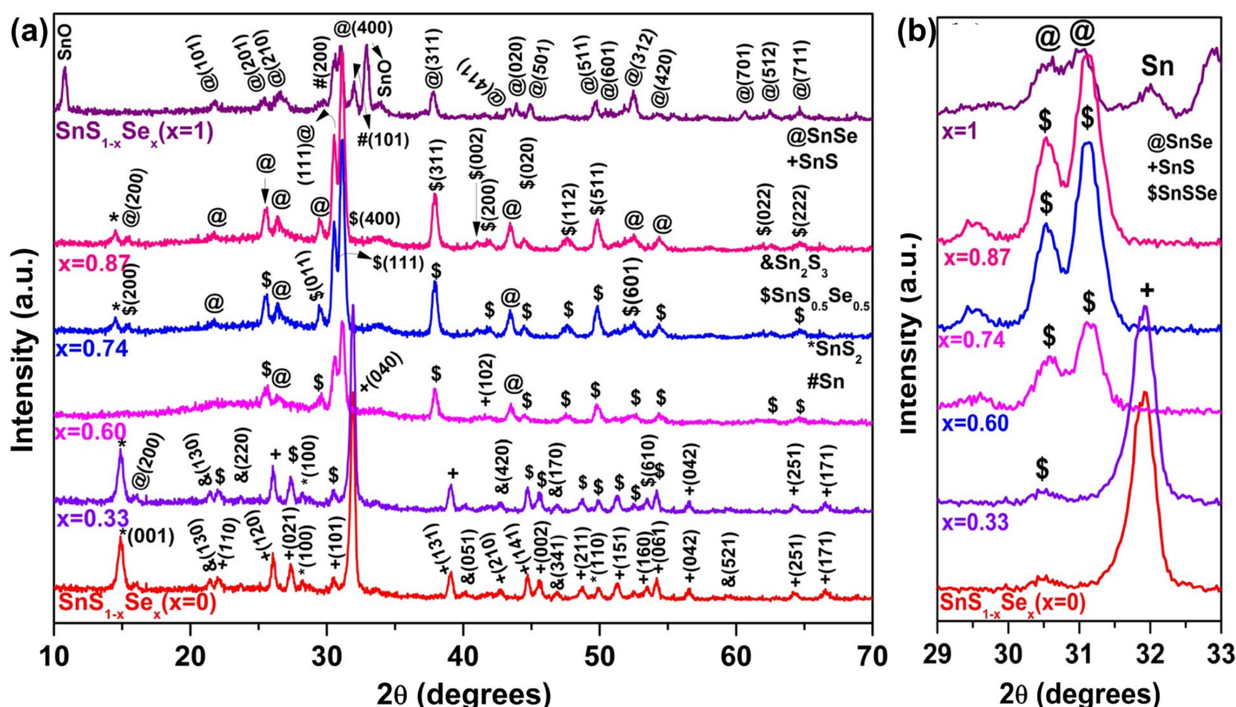

Figure 2: XRD plots for changed Se ($x=0$ to 1) composition in MSELD $SnS_{1-x}Se_x$ stack films for 2θ ranges varied from a) 10°–70° (b) 29°–33°.

TABLE 2: Different Structural parameters with changed Se content in SnS film.

Composition	+(040)/@$(400)	Intensity	*(001)/#(101)	Intensity	Cell parameters (Å)	Volume (Å^3)
$SnS_{1-x}Se_x$ ($x=0$)	31.91+	960	14.87	300	($a=4.31$; $b=11.21$; $c=3.995$)+ ($a=8.77$; $b=14.11$; $c=3.688$)& ($a=b=3.53$; $c=5.95$)*	193.01 +
$SnS_{1-x}Se_x$ ($x=0.33$)	31.915+	960	14.875	300	($a=4.32$; $b=11.21$; $c=3.97$) + ($a=11.49$; $b=3.81$; $c=4.62$)$	192.25 + 202.25$
$SnS_{1-x}Se_x$ ($x=0.60$)	31.105$	916	14.515	104	($a=11.49$; $b=4.17$; $c=4.394$) $	201.90$
$SnS_{1-x}Se_x$ ($x=0.74$)	31.105$	487			($a=11.48$; $b=4.43$; $c=4.14$) $	210.51$
$SnS_{1-x}Se_x$ ($x=0.87$)	31.135$	921	14.515	104	($a=11.48$; $b=4.43$; $c=4.14$) @	210.57@
$SnS_{1-x}Se_x$ ($x=1$)	31.075@	350	32.005	188	($a=11.50$; $b=4.17$; $c=4.41$) @	211.329@

+SnS (Sys: Orthorhombic, S. G.: Pnma, Cell Parameters (Å): $a=4.33$; $b=11.19$; $c=3.98$)

&Sn_2S_3 (Sys: Orthorhombic, S. G.: Pnam, cell Parameters (Å): $a=8.86$; $b=14.02$; $c=3.747$)

*SnS_2 (Sys: Hexagonal, S. G.: P $\bar{3}$ m1, Cell Parameters (Å): $a=b=3.648$; $c=5.899$)

$$SnS_{0.5}Se_{0.5}$ (Sys: Orthorhombic, S. G.: Pnma, Cell Parameters (Å): $a=11.33$; $b=4.047$; $c=4.376$)

@SnSe (Sys: Orthorhombic, Space Group: Pnma, Cell Parameters (Å): $a=11.497$; $b=4.15$; $c=4.44$)

© The Author(s), under exclusive licence to The Materials Research Society 2021

formation confirmed on the basis of most significant peaks (MSPs) at 2θ values of 31.915°, 26.035° and 39.115° indexed as (040), (120) and (131) planes as per JCPDS card no 39-0354. Moreover, the presence of other secondary phases i.e. SnS_2 (Sys: Hexagonal; S. G.: P $\overline{3}$ m1) corresponding to (001) plane at 2θ value of 14.875° and Sn_2S_3 phase (Sys: Orthorhombic; S. G.: Pnma) has been observed at 2θ value of 21.415°, 46.855° and 59.455° corresponding to (130), (341) and (521) planes identified on the basis of their respective JCPDS. The existence of SnS_2 and Sn_2S_3 peaks result due to decomposition of SnS phase and re-evaporation of 'S' from top of the formed SnS phase due to stronger vapour pressures and leads to the formation of sulphur rich phases at the interface layers. The deposition of lower thickness of 'Se' ($SnS_{1-x}Se_x$; $x=0.33$) on SnS mixture using MSELD results in the formation of ternary $SnS_{1-x}Se_x$ peaks. However, the dominance of SnS phase alongwith the presence of low intensity (001) SnS_2 peak is observed. Thus, the dominated SnS phase maintains its character with the presence of Sn_2S_3 phase. This presence of SnS phase is due to the less availability of 'Se' atoms and, thus, causes lower diffusion into SnS and, exhibit partial transformation of SnS into $SnS_{1-x}Se_x$ phase. The lower 'Se' deposition on the SnS mixture causes growth of $SnS_{1-x}Se_x$ phase at the interface of the MSEL deposited stack of SnS and 'Se'. Such interaction of 'Se' atoms with SnS at 623 K annealing temperature unable to transform the 'Sn' rich layer into $SnS_{1-x}Se_x$ completely due to the less availability of 'Se' atoms deposited at the top of SnS. Thus, the dominance of SnS phase seen to extinct at $SnS_{1-x}Se_x$; $x=0.60$ and exhibit prominent ternary $SnS_{1-x}Se_x$ phase alongwith some minor SnSe peaks. This dominance of $SnS_{1-x}Se_x$ phase might be due to higher diffusion of 'Se' atoms into SnS lattice from top interface to bottom as compared to the film S2. Besides this, the existence of SnSe phase is due to the re-evaporation of 'S' atoms from top of the layer due to higher temperature. The effect of annealing temperature behaviour for $x=0.60$ films by changing the temperature from 473 to 623 K has already been reported previously [24]. A complete conversion of SnS peaks to $SnS_{1-x}Se_x$ peaks were observed for $x=0.74$ as per the peaks at 2θ values of 30.415°, 21.985° and 53.515° indexed to (011), (114) and (610) planes. Apart from these, peaks corresponding to SnSe phase at 2θ values of 26.435° and 43.435° indexed to (210) and (020) planes were also observed alongwith a slight presence of SnS_2 peak corresponding to (001) plane. The complete transformation of SnS into $SnS_{1-x}Se_x$ at $x=0.77$ has been seen as there is no other peaks of SnS were observed. Besides this, peaks of SnSe binary phase observed due to re-evaporation of 'S' from the top. Further, the increase in $x=0.87$ results in increase of the SnSe peaks with the dominance of $SnS_{1-x}Se_x$ phase alongwith the presence of SnS_2 peak. The presence of SnS_2 phase is due to the reaction of the evaporated 'S' and causes the formation of sulphur rich phase due to its facile character. Moreover, higher 'Se' concentration leads to cause doping at substitutional sites and hence shows unchanged 2θ position corresponding to MSP (most significant peak).

Thus, a complete transformation from SnS to SnSe has been achieved by doping 'Se' atoms into SnS phase with different stoichiometric ratios through $SnS_{1-x}Se_x$ upto S5. At $x=1$, $SnS_{1-x}Se_x$ results into SnSe phase along (040), (201) and (311) planes corresponding to 2θ values 31.075°, 25.435° and 37.825° as per JCPDS card no 48–1224. The impurity phase corresponding to SnO phase were also observed due to improper reaction of the precursor 'Sn' and 'Se' layers which needs to be optimized.

The magnified view of $SnS_{1-x}Se_x$ ($x=0$ to 1) films in the 2θ range 29°–33° has been presented in Fig. 2b and a conclusion has been drawn that films showed dominance of SnS phase upto $x=0.33$ due to the lower presence of 'Se' content in the films presenting partial transformation of SnS lattice to $SnS_{1-x}Se_x$. While a sharp transition in the form of peak shift from 31.915° to 31.075° corresponding to MSP signifies the structural engineering from SnS into $SnS_{1-x}Se_x$ that correspond to the deeper level interaction of 'Se' atoms into the already present SnS lattice, thus, causes decrease in the crystallinity of the film. Moreover, a similar behaviour for prominent peak corresponding to $x>0.60$ has been observed with slight variations in the 2θ values due to the formation of other mixed binary phases. These changes in dominance of the peak demonstrate phase variations due to the incorporation of the 'Se' atoms more deep inside the SnS lattice. The unit cell parameter calculation for the $SnS_{1-x}Se_x$ ($x=0$ to 1) presents variation in the lattice parameters calculated corresponding to the most prominent peaks using Eq. (1) [45].

$$\frac{1}{d^2}=\frac{h^2}{a^2}+\frac{k^2}{b^2}+\frac{l^2}{c^2} \quad (1)$$

A significant change in the cell parameters on varied 'Se' layer of the films has been observed and presented in Table 2. The films of composition $SnS_{1-x}Se_x$; $x=0$ showed the lattice parameters aggregate to SnS JCPDS values. However, conversion of phases from SnS to $SnS_{1-x}Se_x$ leads to the changes in cell parameters and exhibit consistent modifications to their reported JCPDS values due to varied 'Se' constituents in the films. These modifications in the structure has also been noted from volume size of the cell which increases with the increase in the 'Se' constituent and found to have maximum volume ~ 211.33 $Å^3$ corresponding to SnSe phase as presented in Table 2. The lower value of volume size upto S2 was observed due to dominance of SnS phase alongwith the presence of SnS_2 and $SnS_{1-x}Se_x$ phase. Moreover, the linear increase in the unit cell volume is in accordance with the Vegard's law, indicating the replacement of smaller 'S' atoms by larger 'Se' atoms causing increased unit cell volume. This increased volume size attributed to the complete insertion of higher atomic radii in place of 'S' atoms thoughout the whole SnS lattice and diminishes SnS character in the films. Thus, structural parameter engineering

© The Author(s), under exclusive licence to The Materials Research Society 2021

results into tuning of various spectral selective characteristics over the NIR region for their use as sensors and tuners in photonic applications. These variations in volume size has been confirmed from consistent variations in the unit cell volume in between SnS (192.84 Å^3) and SnSe (211.84 Å^3) phase as per JCPDS values.

The films obtained without 'Se' ($SnS_{1-x}Se_x$; $x=0$) layer doping exhibits higher crystalline nature ~ 29.7 nm. This higher crystallite size in the SnS film exhibit the growth achieved due to higher annealing temperature. However, the doping ($x=0.33$) disturbs the crystallite size due to the insertion of larger atomic radii into SnS lattice and thus, cause lower decrease in the crystallite size to 29.3 nm attributed to the less distortions produced in the crystal structure due to partial insertion of 'Se' atoms into SnS lattice. The film $x=0.60$ show significant decrease in the crystalline quality of SnS attributed to the higher diffusion of 'Se' atoms due to differences in the effective ionic radii of Se^{2-} (1.98 Å) and S^{2-} (1.84 Å) and thus leads to lattice mismatch and lattice distortions causing deformation in the cell structure, lattice parameters and increase in cell volume. However, further increase in 'Se' concentration exhibits increased grain growth attributed to complete diffusion of 'Se' atoms achieved and leads to enhancement of crystal growth at higher annealing temperature.

The addition of foreign atoms (Se) in the well formed lattice structure leads to defect formation and causes strain (ε_{zz}) along different axis in the original lattice. This axis strain in the deformed lattice due to insertion of 'Se' atoms has been evaluated using Eq. (2) [46].

$$\varepsilon_{zz}(\%) = \left(\frac{c - c_0}{c_0}\right) \times 100 \quad (2)$$

where c is the strained lattice parameter calculated from the X-ray diffraction data along a, b, & c axis, respectively and c_0 is the unstrained lattice parameter along respective axis of bulk SnS and $SnS_{0.5}Se_{0.5}$ as presented in Table 3. Thus, changed 'Se' concentration in the deposited thin films causes variation in the axis strain. But the value of this axis strain due to the presence of defects is very small. This type of behaviour has been observed for S1 films in which the films showed a lower value of axis strain due to SnS phase formation. The presence of small values of axis strain for S1 films may arise due to the emergence of defects produced by presence of polytypic SnS phases in the film. The small incorporation of larger atomic radii atoms in the already existing SnS lattice leads to increased axis strain. The increase in the value of axis strain due to the insertion of 'Se' atoms causes disturbance in the crystal structure. The increase in 'Se' concentration leads to further increase in axis strain ($SnS_{1-x}Se_x$, $x=0.60$). Beyond $x>0.60$, the films showed unchanged axis strain. This unchanged axis strain parameters attributed to the complete transformation of SnS into $SnS_{1-x}Se_x$. This happens as structure reached its stable state and demonstrates in the form of unchanged dominant plane 2θ value of 31.1°. Thus, 'Se' atoms further unable to diffuse in SnS lattice sites and results in formation of ternary $SnS_{1-x}Se_x$ phase in the form of a solid solution. However, diffusion of 'Se' atoms stops as the lattice reaches its stable state and unable to permit further replacement in SnS lattice on originating vacancy caused due to 'S' vacancies or re-evaporation. Moreover, the changes in the axis strain values corresponding to SnS phase, $SnS_{1-x}Se_x$ phase and SnSe has also been observed which might be attributed to the thermal disturbances caused by higher annealing temperature. The films of composition $SnS_{0.67}Se_{0.33}$ showed lower axis strain corresponding to SnS phase whereas the axis strain corresponding to $SnS_{0.5}Se_{0.5}$ and SnSe phase is higher.

Thus, reveals the penetration of SnS lattice and replacement of 'S' atoms with higher atomic radii 'Se' atoms having dominant SnS character. However, the axis strain found to be increased with increased 'Se' concentration in the existing lattice calculated corresponding to SnS phase. While the axis strain found to be changed and exhibit lower axis strain for $x=0.60$ evaluated corresponding to SnSe phase. However, for $x=0.74$ and 0.87, the axis strain value is found increased in view of $SnS_{1-x}Se_x$ and SnSe phase and also reveals the formation of ternary lattice which differ from $SnS_{0.5}Se_{0.5}$ phase. Moreover, the lattice corresponding to $x=1$ possess smaller value of axis strain that corresponds to the presence of other Sn and SnO phases. This axis strain comparison reveals the change in phase from SnS to SnSe through $SnS_{1-x}Se_x$ and leads to display changed optical properties.

The thicknesses of the films after annealing were also measured by using surface profilometry (physical measurement). The

TABLE 3: Comparison of axis strain values with the JCPDS data of SnS, $SnS_{0.5}Se_{0.5}$ and SnSe.

Composition	Axis strain to SnS	Axis strain to $SnS_{0.5}Se_{0.5}$	Axis strain to SnSe
$SnS_{1-x}Se_x$ ($x=0$)	0.46 (*a*); 0.178(*b*); 0.376(*c*)	–	–
$SnS_{1-x}Se_x$ ($x=0.33$)	0.23 (*a*); 0.178(*b*); 0.23(*c*)	1.412 (*a*); 5.78 (*b*); 5.575 (*c*)	0.06 (*a*); 8.19 (*b*); 4.054 (*c*)
$SnS_{1-x}Se_x$ ($x=0.60$)	2.68 (*a*); 4.27(*b*); 1.478 (*c*)	1.412 (*a*); 3.039 (*b*); 0.411 (*c*)	0.06 (*a*); 0.482 (*b*); 1.036(*c*)
$SnS_{1-x}Se_x$ ($x=0.74$)	2.59 (*a*); 2.309(*b*); 4.02 (*c*)	1.32 (*a*); 9.46 (*b*); 5.39(*c*)	0.147 (*a*); 6.74(*b*); 6.756 (*c*)
$SnS_{1-x}Se_x$ ($x=0.87$)	2.59 (*a*); 2.309(*b*); 4.02 (*c*)	1.32 (*a*); 9.46 (*b*); 5.39(*c*)	0.147 (*a*); 6.74(*b*); 6.756 (*c*)
$SnS_{1-x}Se_x$ ($x=1$)	–	–	0.05 (*a*); 0.48 (*b*); 0.675 (*c*)

© The Author(s), under exclusive licence to The Materials Research Society 2021

films were found to posses varied thicknesses with change in 'Se' layer deposition. Both the thicknesses measured from DTM and profilometry were presented in Table 4 and found to have variation in the film thickness measured during evaporation and post annealing. The films found to have higher variation for the film thickness of post annealing due to the presence of higher 'Se' content in the layer which deformed the lattice and increases the volume size adversely with increase in film thickness.

TABLE 4: Variation in phases and thickness of MSEL deposited films before and after annealing.

Composition	Phases present	Thickness in nm (Measured using) Before annealing (DTM)	After annealing (surface profiler)
$SnS_{1-x}Se_x$ ($x=0$)	SnS, Sn_2S_3, SnS_2	600	605
$SnS_{1-x}Se_x$ ($x=0.33$)	SnS, Sn_2S_3, SnS_2, SnSSe	450	449
$SnS_{1-x}Se_x$ ($x=0.60$)	SnS, SnS_2, SnSSe, SnSe	600	603
$SnS_{1-x}Se_x$ ($x=0.74$)	SnSSe, SnSe	700	720
$SnS_{1-x}Se_x$ ($x=0.87$)	SnS_2, SnSSe, SnSe	830	852
$SnS_{1-x}Se_x$ ($x=1$)	Sn, SnSe, SnO	400	407

Optical characteristics of post annealed MSELD $SnS_{1-x}Se_x$ stack alloy thin films

The optical results measured in Vis–NIR region of the EM spectrum in transmission (T%) mode has been presented in Fig. 3a. The SnS films ($SnS_{1-x}Se_x$; $x=0$) showed higher transmission (T%), moreover, the incorporation of 'Se' atoms ($SnS_{1-x}Se_x$; $x=0.33$) leads to a consistent decrease in the transmission (T%) attributed to the defect states arises due to the lattice mismatch. However, a red shift in the transmission edges towards higher wavelength side in the near infrared region of the EM spectrum has been observed. Further, increase in selenium content leads to decrease in the transmission (T%) corresponding to $SnS_{1-x}Se_x$ phase and found to have lower transmission for SnSe films. This decrease in the transmission (T%) is attributed to the insertion

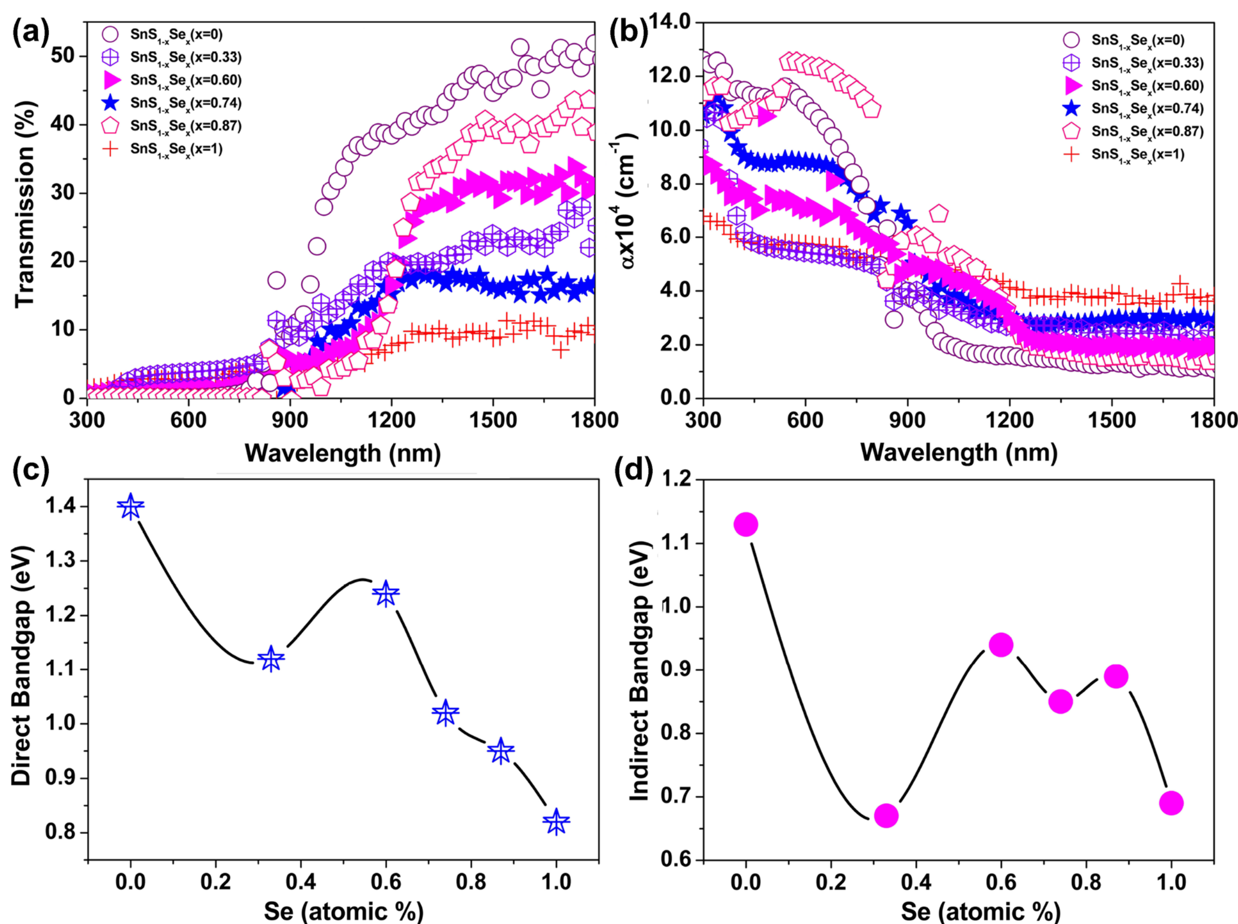

Figure 3: Optical results of the varied $SnS_{1-x}Se_x$ stack film compositions showing variation in (a) Transmission verses wavelength b) Absorption Coefficient versus wavelength, (c) Direct bandgap and (d) Indirect bangap using UV–Vis–NIR spectrophotometer.

© The Author(s), under exclusive licence to The Materials Research Society 2021

of 'Se' atoms in SnS. While a lower transmission (T%) in SnSe films might be due to the presence of oxide and 'Sn' phases (secondary) in the films.

The transmission (T%) curves of different MSEL deposited stacks of 'Se' concentration ($SnS_{1-x}Se_x$; $x = 0$, 0.33, 0.60, 0.77, 0.87, 1) has been used for the calculation of absorption coefficient (α) using Eq. (3) [47].

$$\alpha = \frac{1}{t}\ln\left(\frac{100}{T\%}\right) \tag{3}$$

where t is the film thickness.

The obtained results for absorption coefficient versus wavelength are presented in Fig. 3b. A distinction in the edge sharpness has been observed corresponding to changed composition. The $SnS_{1-x}Se_x$ ($x = 0.33$) showed sharp transitions while further increase in the composition yields increased flatter response of absorption edge. Moreover, the SnS films showed higher absorption coefficient value ~ 1×10^5 cm^{-1} which decreases due to the insertion of 'Se' atoms and causes imperfections and disturbances in the energy bands. However, further increase in 'Se' concentration demonstrates increase in the absorption and found to exhibit higher absorption coefficient value for $SnS_{0.13}Se_{0.87}$ films. This increase in absorption value may be attributed to the increased thickness of the film caused due to increase in 'Se' layer thickness and also higher structural stability and lower axis strain corresponding to SnSe. Thus, the films showed higher photosensitivity for the films having SnS phase (S1), $SnS_{0.67}Se_{0.33}$ (S2) and $SnS_{0.87}Se_{0.13}$ (S5) to those of other compositions. In addition, the film found to exhibit higher absorption over the NIR to UV region of the EM spectrum and finds its suitability as a absorber layer in solar cell technology. These absorption coefficient values as a function of wavelength have been used to calculate bandgap of the films using Eq. (4) [48].

$$\alpha h\nu = B\left(h\nu - E_g\right)^{\frac{1}{n}} \tag{4}$$

where n is 2 and 1/2 for direct and indirect band transitions respectively, B; proportionality constant and hν; photon energy. Direct bandgap for MSEL deposited different $SnS_{1-x}Se_x$ film compositions has been evaluated by plotting a graph of $(\alpha h\nu)^2$ versus $h\nu$ on extrapolating the values to $h\nu = 0$ on x-axis.

The calculation of direct bandgap exhibits tuning from 1.40 to 0.82 eV with changed 'Se' concentration in the ($SnS_{1-x}Se_x$) film of varied compositions refer Fig. 4a. The increase in 'Se' layer thickness in MSEL deposited films results into the decrease in the direct bandgap values from 1.4 to 0.82 eV as already reported by various authors. This decrease in the bandgap value has been attributed to the diffusion of 'Se' atoms into orthorhombic SnS lattice and results into conversion of existing SnS phase to ternary $SnS_{1-x}Se_x$ with changed MSEL deposited stack compositions. However, a comparatively lower bandgap value for $x = 0.33$ was observed due to the presence of mixed phases of SnS, SnS_2, Sn_2S_3 and $SnS_{1-x}Se_x$ corroborated with the x-ray diffraction results. While the bandgap values for higher 'Se' composition yields a consistent decrease in the bandgap value due to the conversion of SnS phase towards SnSe with increased 'Se' content in $SnS_{1-x}Se_x$ alloy. This decrease in the bandgap with the increased 'Se' concentration has been attributed to the phase transformation from SnS (1.3 eV) to SnSe (1.1 eV) and, thus, demonstrates bandgap modulation while transforming SnS to SnSe phase. The change in indirect bandgap value has been evaluated on extrapolation of $(\alpha h\nu)^{1/2}$ versus $h\nu$ plot to $h\nu = 0$ on x-axis refer Fig. 4b. A variation in the indirect bandgap values with the change in 'Se' concentration has also been observed. The obtained varied composition showed a comparatively lower value of indirect bandgap as compared to their direct counterparts. This lower indirect bandgap values releases lower energy in the form of photons thus, have the capability to absorb better as also seen in $SnS_{1-x}Se_x$ ($x = 0.87$) S5. A large decrease in the value of direct and indirect bandgap for $x = 0.33$ concentration might be due to the presence of polytypic SnS (SnS_2 and Sn_2S_3) phases in the films upto composition $SnS_{1-x}Se_x$ ($x = 0.87$). Further, deviations from the standard fit of the bandgap might also be attributed to the presence of other secondary phases in the films as presented in Fig. 3c and d.

This decrease in optical bandgap values also leads to stress reduction in the annealed films because of linearly oriented film surfaces. To confirm the composition value of ternary alloy, theoretically Vegard's law is prominent to establish the film composition from optical study of the films. According to the extended Vegard's law, the empirical energy bandgap relation with changed composition ratio of alloyed materials can be predicted; the bandgap of $SnS_{1-x}Se_x$ nanocrystals can be calculated from the generalized Eq. (5) and presented in Table 5 [49, 50].

$$E_g^{SnSSe}(x) = (1-x)E_g^{SnS} + xE_g^{SnSe} - bx(1-x) \tag{5}$$

where b refers to the specific "Optical bowing constant" which describes the degree of nonlinearity. However, in present case, the value of b is slightly higher that might arise due to some nonlinear character due to presence of mixed phases (SnS_2, Sn_2S_3) in the alloy films. The calculated bandgap is 1.097 eV for $SnS_{1-x}Se_x$ ($x = 0.33$), while the bandgap value decreases to 0.815 eV for the composition value of $SnS_{1-x}Se_x$ ($x = 0.87$). These changes thus, explain the variation of bandgap due to the replacement of 'S' with 'Se' which influences the distribution of electronic structure in the whole film. The bandgap values calculated using Vegard's law with changed 'Se' composition corroborate well with the experimental bandgap values calculated from UV–Vis–NIR with minor variations. These variations in the bandgap values

© The Author(s), under exclusive licence to The Materials Research Society 2021

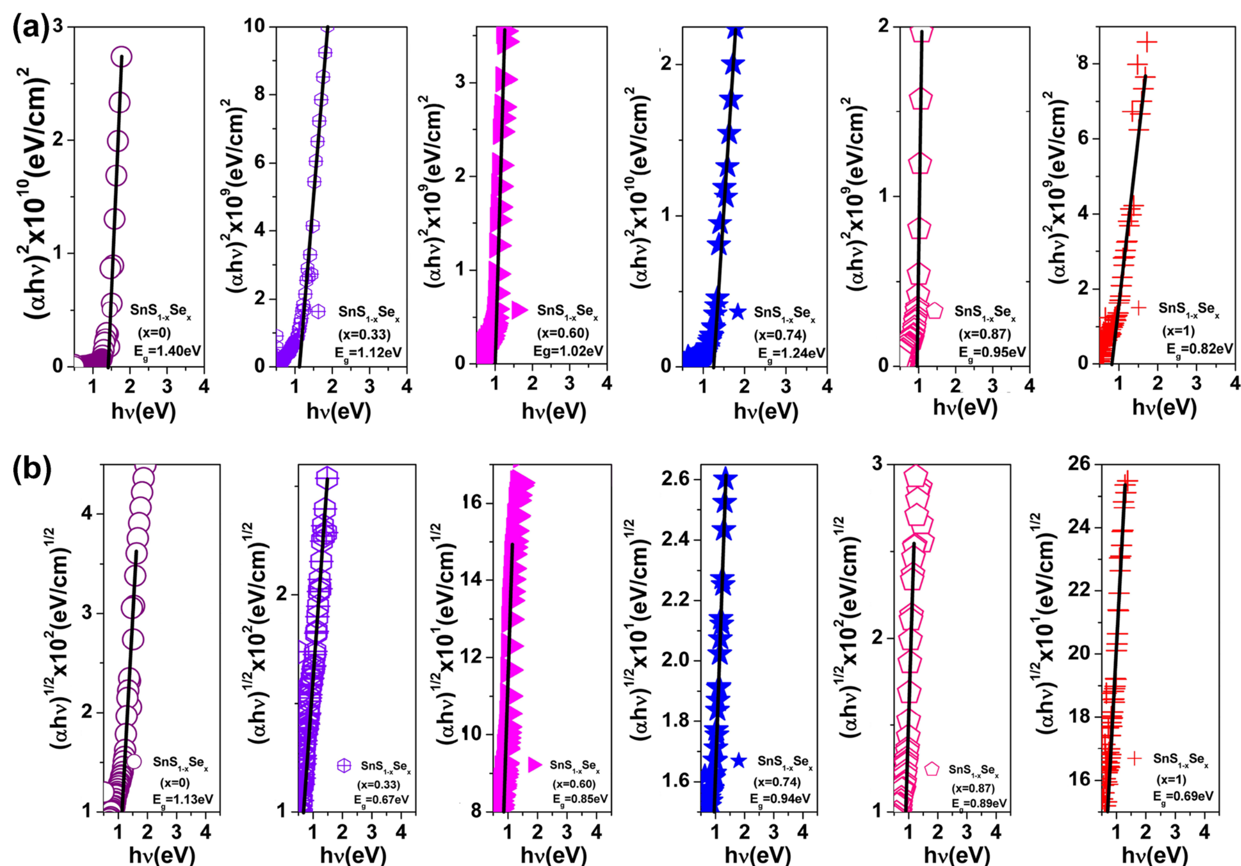

Figure 4: (a) $(ahv)^2$ versus wavelength of the selenium doped $SnS_{1-x}Se_x$ stack films. (b) $(ahv)^{1/2}$ versus wavelength of the selenium doped $SnS_{1-x}Se_x$ stack films.

TABLE 5: Various optical parameters of the selenium doped SnS thin films.

Composition	Direct bandgap (eV)	Vegard's law Eg (eV)	Indirect bandgap (eV)	Absorption coefficient value (cm^{-1})
$SnS_{1-x}Se_x$ ($x=0$)	1.40	1.40	1.13	1.1×10^5
$SnS_{1-x}Se_x$ ($x=0.33$)	1.12	1.097	0.67	5.4×10^4
$SnS_{1-x}Se_x$ ($x=0.60$)	1.02	1.002	0.85	8.0×10^4
$SnS_{1-x}Se_x$ ($x=0.74$)	1.24	0.876	0.94	8.7×10^4
$SnS_{1-x}Se_x$ ($x=0.87$)	0.95	0.815	0.89	1.2×10^5
$SnS_{1-x}Se_x$ ($x=1$)	0.82	0.82	0.69	4.7×10^4

in comparison to the bandgap calculated from Vegard's law is due to the presence of other binary phases in the films along with the dominant $SnS_{1-x}Se_x$ phase.

The changes in 'Se' concentration in $SnS_{1-x}Se_x$ alloy films showed variation in the extinction coefficient values as a function of wavelength as shown in Fig. 5a. The films exhibit higher surface smoothness in the wavelength > 1000 nm in terms of lower value of extinction coefficient (K). However, the films present higher value of extinction coefficient in the visible region of the EM spectrum. On 'Se' substitution, the film exhibit a lower value in the visible region in comparison to SnS phase while the films present still higher K in wavelength > 1000 nm. However, further increase in 'Se' concentration showed higher value of extinction coefficient as compare to $SnS_{1-x}Se_x$ ($x=0.33$) for S2 film. The films having higher 'Se' concentration results into higher value of extinction coefficient. This increased K results due to the increased 'Se' concentration attributed to the higher rate of diffusion into SnS lattice and thus produces defects on the surface of the films. Moreover, a tuned surface smoothness has also been observed with changed 'Se' concentration. Thus, the transformation of SnS to SnSe results in the lower surface smoothness with the insertion of surface 'Se' atoms deep inside into SnS lattice. The $SnS_{1-x}Se_x$ ($x=1$) films corresponding to SnSe films showed higher K value due to the presence of Sn, SnO phases in the film.

The varied composition ($SnS_{1-x}Se_x$) films were also undertaken for optical measurements in energy mode with changed wavelength and shown in Fig. 5b. The $SnS_{1-x}Se_x$ films were seen to

© The Author(s), under exclusive licence to The Materials Research Society 2021

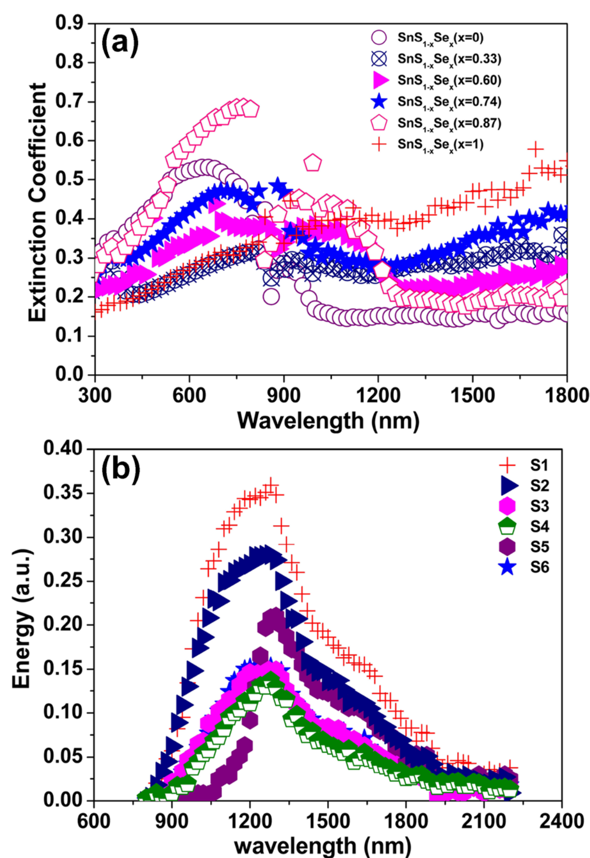

Figure 5: Plots showing $SnS_{1-x}Se_x$ stack films with changed selenium composition as function of wavelength for (a) extinction coefficient (b) energy mode measurement using UV–Vis–NIR spectrophotometer.

exhibit higher energies over a broad range of wavelengths ranging from 800 to 1400 nm, hence, depicts its utility as photo sensitive layer for sensing application. The varied composition ($SnS_{1-x}Se_x$) however, shows a hump in the wavelength range 1400 nm to 1600 nm. This might be due to the presence of indirect bandgap lies in this wavelength range caused due to polytypic mixed phases. Besides this, deposition of 'Se' layer on SnS, showed lower radiative energy phenomenon in terms of intensity and spectral region which decreases further with varied composition of the film. Moreover, the films exhibit a shift in the spectral edge from 800 to 1100 nm with changed film composition. Thus, the $SnS_{1-x}Se_x$ annealed films exhibit changed sensing wavelength as well as capacity on varied composition from SnS to SnSe, thus, depicting its changed sensing capability for various photonic applications in NIR region of the spectrum.

Morphology of post annealed MSELD $SnS_{1-x}Se_x$ stack alloy thin films

Figure 6 presents the SEM images of varied $SnS_{1-x}Se_x$ film compositions deposited using facile MSELD technique. The surfaces of the films are found to be free from pinhole, cracks in which grains were distributed uniformly over the entire surface. The film S1 showed uniform spherical and homogeneous grains corresponding to SnS phase. However, the varied 'Se' concentration results in darker crystallites, this may also be confirmed from the deposition analogy where 'Se' layer has been deposited at the top. While the appearance of brighter crystallites reveals the growth of $SnS_{1-x}Se_x$ grains at the top due to the interlayer diffusion of 'Se' atoms from top to the bottom of SnS lattice.

Hall measurements of post annealed MSELD stack of $SnS_{1-x}Se_x$ alloy thin films

The films found to show higher value of sheet resistivity as compared to the bulk resistivity of the deposited MSELD films of varied composition (Table 6). These high values of the sheet resistivity of the films (S1 to S5) are attributed to the presence of more surface states that induces defects. Besides this, the film S6 showed relatively lower sheet resistivity value due to the lower presence of defect states in the film. The higher presence of sheet resistivity might also be due to the presence of strain in the film induced in SnS lattice. Moreover, the value of sheet resistivity is small and lies in the range of 4.5 to 66.9 Ω/sq for the films S1 to S5 whereas the film S6 found to have lower resistivity value of 5.06×10^{-2} Ω/sq. Such a lower value of resistivity attributed to the presence of higher metallic content in the film as compared to other SnS and $SnS_{1-x}Se_x$ films. The films found to exhibit increase and decrease in the value of resistivity. These changes in the values of the resistivity might be attributed to the variations in the composition alongwith the presence of mixed phases in the film. The mobility of the films has been found to vary in the range 1.8 to 9.8 $cm^2/(V{\cdot}s)$ for SnS and $SnS_{1-x}Se_x$ films while a higher value of mobility 784.6 $cm^2/(V{\cdot}s)$ has been observed for SnSe films. This higher value might be attributed to the presence of higher metallic and oxide content present in the films. However, the carrier concentration has been observed to vary from 1.12×10^{16} to 1.57×10^{17} cm^{-3}. The carrier concentration of SnS films has been observed to be 1.12×10^{16} cm^{-3} and found to increase due to the incorporation of 'Se' atoms in SnS and exhibit the value of 1.57×10^{17} cm^{-3}. Further increase in dopant (Se atoms) decreases carrier concentration for $SnS_{0.13}Se_{0.87}$ alloy films. This decrease in the value of carrier concentration attributed to the stable $SnS_{1-x}Se_x$ alloy formation which didn't permit further doping of 'Se' in SnS lattice due to saturation of Se diffusion. The SnSe films also exhibit higher concentration value ~ 1.57×10^{17} cm^{-3}. Moreover, the ($SnS_{1-x}Se_x$ $x = 1$) films shows higher concentration as has also been observed and corroborated well with the EDAX and structural results. Thus, the deposited varied MSELD stack films exhibit excellent electrical parameters viz. Bulk resistivity (4.5 to 66.9 Ωcm), mobility (1.8–9.8 cm^2/Vs) and carrier concentration (~ 10^{16}–10^{17} cm^{-3})

Journal of Materials Research Volume 36 Issue 17 September 2021 www.mrs.org/jmr

© The Author(s), under exclusive licence to The Materials Research Society 2021

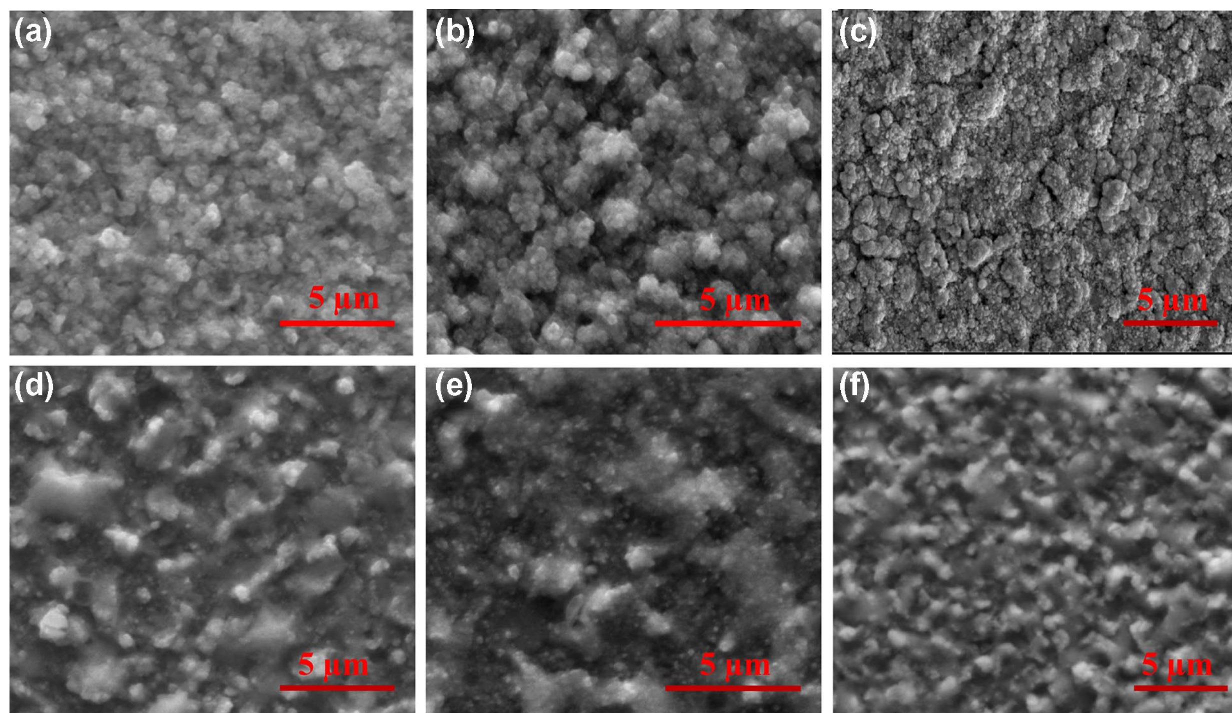

Figure 6: SEM images obtained on annealing of MSELD thin films of the (a) SnS (b) $SnS_{0.67}Se_{0.33}$ (c) $SnS_{0.40}Se_{0.60}$ (d) $SnS_{0.26}Se_{0.74}$ (e) $SnS_{0.13}Se_{0.87}$ and (f) SnSe films.

TABLE 6: Variation of electrical parameters with changed Selenium composition on SnS thin films.

Sample	Sheet resistivity (Ω/sq)	Bulk resistivity (Ωcm)	Mobility $cm^2/(V\ s)$	Carrier concentration (cm^{-3})
S1	6.69×10^5	6.69×10^1	8.3	1.12×10^{16}
S2	4.49×10^4	4.49×10^0	8.8	1.57×10^{17}
S3	5.2×10^4	4.10×10^1	6.5	8.72×10^{16}
S4	4.40×10^5	3.96×10^1	1.8	7.95×10^{16}
S5	2.03×10^5	2.03×10^1	9.8	3.15×10^{16}
S6	5.06×10^2	5.06×10^{-2}	784.6	1.57×10^{17}

are optimum for their use as an absorber layer in PV technology for the S1 to S5 films.

Conclusions

Facile phase composition engineering has been achieved for $SnS_{1-x}Se_x$ films using MSELD technique using lab methodology for large production at industrial scale. The structural engineering interpreted on the basis of structural deformation, causes strain and deviations in the unit cell parameters and volume (192.25 Å–211.33 Å), resulted due to the replacement of higher atomic radii 'Se' with lower atomic radii (S). Higher atomic radii insertion causes direct bandgap narrowing varying from 1.40 to 0.82 eV having high absorption ~ 10^5 cm^{-1} in Vis–NIR region for its use as a solar absorber, tuners and photonic sensor applications. The alloy $SnS_{1-x}Se_x$ films found to demonstrate excellent electrical parameters viz. Resistivity (66.9 – 4.49 Ωcm), mobility (1.8 – 9.8 cm^2 / Vs) and carrier concentration (~ 10^{16} to 10^{17} cm^{-3}) for their suitability as an absorber layer in solar cell structure. Thus, the study highlighted facile development of $SnS_{1-x}Se_x$ phase formation at large scale and can be used in the field of optical sensors (Vis–NIR), absorbers, and optical tuners to achieve material suitability in photonic devices.

Materials and methods

Highly pure 'Sn', 'S' and 'Se' powders procured from sigma Aldrich were used as precursor materials for the deposition of varied composition films. The films were deposited using multisource thermal evaporation (Make: Hindhi Vac, India;

© The Author(s), under exclusive licence to The Materials Research Society 2021

Model: 12A4DM) in a sequential manner at a base vacuum pressure of 2×10^{-6} mbar. The powder material was kept in two sources (Molybdenum boats); one having mixture of 'Sn' and 'S' while other having 'Se' powder. The study of SnS mixture deposition with varied composition, thickness and annealing temperature has already reported [51–53]. The present MSELD technique used to achieve $SnS_{1-x}Se_x$ alloy by varying 'Se' layer concentration and leads to formulation of different stoichiometric ratios of 'Sn', 'S' and 'Se' constituents in the form of a solid solution by depositing varied stoichiometric weight percentages. The films were deposited on organically cleaned corning glass substrates in a hot ultrasonic bath cleaner using trichloroethylene, acetone and methanol (TAM). During deposition, the distance between source to substrate, crystal to substrate; rate of evaporation (~ 3 Å/s) and substrate rotation were kept constant. The rate of evaporation monitored using digital thickness monitor (Make: HindhiVac, India; Model: DTM 101). The cumulative thickness of the MSELD deposited films using DTM has been found to be 600 nm, 450 nm, 600 nm, 700 nm, 830 nm and 400 nm indexed as S1, S2, S3, S4, S5 and S6. The resultant films were annealed at 623 K in a tubular furnace under the vacuum ~ 1×10^{-3} mbar for one hour (h) to obtain the solid state reaction between Sn, S and Se deposited constituent layers.

Characterization

For structural parameters, the X-ray diffraction data has been collected in a line scan mode in 2θ range 10°–70° using GIXRD (Grazing incident X-ray diffractometer). The incident X-rays filtered using $CuK\alpha_1$ radiation ($\lambda = 1.5406$ Å) in a powder X-ray diffractometer equipped with HD Bragg Brentano incident geometry (Make: PANalytical; Model: X'pert^3 powder). During measurements, step size of 0.03° and time per step of 0.15 / sec(s) were used for data collection at a grazing incidence angle of 1.7°. The surface morphology of the films has been determined by using field emission scanning electron microscope (FESEM) (Make: JFEI; Model: Nova Nano SEM-450) while the composition of the constituent materials established from energy dispersive X-ray analysis (EDAX) attachment of SEM which confirmed the formulation of $SnS_{1-x}Se_x$ in the form of alloy. The films have been undertaken for optical analysis; the transmittance and energy spectral response of the films obtained by using UV–Vis–NIR spectrophotometer (Make: Shimadzu; Model: UV-3600) in the wavelength range 300 to 1600 nm at room temperature. The thicknesses of the deposited films were calculated by using surface profilometery (make: Vecco).

Data availability

The data sets generated during the current study are not publically available to the First time synthesis of such alloys but are available from the corresponding author on reasonable request.

Declarations

Conflict of interest The authors do not have any conflict of interest.

References

1. P. Sinsermsuksakul, J. Heo, W. Noh, A.S. Hock, R.G. Gordon, Adv. Energy Mater. **1**, 1116 (2011)
2. B. Ghosh, R. Battacharjee, P. Banerjee, S. Das, Appl. Surf. Sci. **257**, 3670 (2011)
3. O.E. Ogah, G. Zoppi, I. Forbes, R.W. Miles, Thin Solid Films **517**, 2485 (2009)
4. S. Kim et al., Sol. Energy Mater. Sol. Cells **119**, 26–35 (2013)
5. T.D. Lee, A.U. Ebong, Renew. Sustain. Energy Rev. **70**, 1286 (2017)
6. I. Masaya, N. Yuki, Jpn. J. Appl. Phys. **48**(E9), 090202 (2009)
7. K. Hironori, S. Kotoe, W. Tsukasa, S. Hiroyuki, K. Tomomi, M. Shinsuke, Sol. Energy Mater. Sol. Cells **65**(E8), 141 (2001)
8. D.B. Mitzi, O. Gunawan, T.K. Todorov, K. Wang, S. Guha, Sol. Energy Mater. Sol. Cells **95**, 1421 (2011)
9. H. Katagiri, K. Jimbo, W.S. Maw, K. Oishi, M. Yamazaki, H. Araki, A. Takeuchi, Thin Solid Films **517**, 2455 (2009)
10. S. Ruhle, Sol. Energy **130**, 139 (2016)
11. W. Wang, M.T. Winkler, O. Gunawan, T. Gokmen, T.K. Todorov, Y. Zhu, D.B. Mitzi, Adv. Energy Mater. **4**(7), 1301465 (2014)
12. W. Shockley, H.J. Queisser, J. Appl. Phys. **32**, 510 (1961)
13. A. Polman, M. Knight, E.C. Garnett, B. Ehrler, W.C. Sinke, Science **352**, 4424 (2016)
14. P. Sinsermsuksakul, L.Z. Sun, S.W. Lee, H.H. Park, S.B. Kim, C.X. Yang, R.G. Gordon, Adv. Energy Mater. **4**, 1400496 (2014)
15. B. Hamad, Journal of Electronic Materials 47 (7), (2018)
16. W. Gao, Z. Zhang, L. Huang, J. Yao, Y. Zhao, Y. Xiao, J. Li, A.C.S. Appl, Mater. Interfaces **11**, 40222 (2019)
17. H. Wei, Y. Su, S. Chen, Y. Lin, Z. Yang, X. Chen, Y. Zhang, J. Mater. Chem. **21**, 12605 (2011)
18. E. Barrios-Salgado, L.A. Rodriguez-Guadarrama, M.L.R. Garcia, L.G. Martinez, M.T.S. Nair, P.K. Nair, Phys. Status Solidi A **1700036**, 1 (2017)
19. W. Albers, C. Haas, H. Ober, G.R. Schodder, J.D. Wasscher, J. Phys. Chem. Solids **23**, 215 (1962)
20. T.H. Patel, R. Vaidya, S.G. Patel, Bull. Mater. Sci. **26**, 569 (2003)

© The Author(s), under exclusive licence to The Materials Research Society 2021

21. B. Subramanian, C. Sanjeeviraja, M. Jayachandran, Mater. Res. Bull. **38**, 899 (2003)
22. V. Dhanasekaran, K. Sundaram, J. Jung, T. Mahalingam, J. Mater. Sci.: Mater. Electron. **26**, 1641 (2015)
23. V. Kumar, D.K. Sharma, K. Sharma, P. Singh, D.K. Dwivedi, J. Mater. Sci.: Mater. Electron. **29**, 846 (2018)
24. A. Banotra, N. Padha, J. Electron. Mater. **47**, 1 (2018)
25. H. Kafashan, Mater. Sci. Semicond. Process. **88**, 148 (2018)
26. K. Saritha, S. Rasool, K.T. Ramakrishna Reddy, A.M. Saad, M.S. Tivanov, S.E. Tikoto, O.V. Korolik, V.F. Gremenok, Appl. Phys. A **125**, 704 (2019)
27. H.S. Im, Y. Myung, Y.J. Cho, C.H. Kim, H.S. Kim, S.H. Back, C.S. Jung, D.M. Jang, Y.R. Lim, J. Park, J.P. Ahn, RSC Adv. **3**, 10349 (2013)
28. H. Ju, M. Kim, D. Park, J. Kim, Chem. Mater. **29**, 3228 (2017)
29. W. Gao, Y. Li, J. Guo, M. Ni, M. Liao, H. Mo, J. Li, Nanoscale **10**, 8787 (2018)
30. L. Tao, B. Yao, P. Wen, Q. Yue, Z. Zhang, Q. Luo, W. Gao, A.C.S. Appl, Nano Mater. **3**, 10270 (2020)
31. A. Ektarawong, B. Alling, J. Phys.: Condens. Matter **30**, 29LT01 (2018)
32. R. Kamada, T. Yagioka, S. Adachi, A. Handa, K. F. Tai, T. Kato, H. Sugimoto, Proc. In: IEEE 43rd Photovoltaic Specialists Conference, (2016) pp. 1287–1291
33. J. Ramanujam, U.P. Singh, Energy Environ. Sci. **10**, 1306 (2017)
34. V. Robles, J.F. Trigo, C. Guillen, J. Herrero, Mater. Chem. Phys. **167**, 165 (2015)
35. J.A. Arvizu, M. Courel, M.G. Sauchez, R. Gonzalez, D. Jnenez, I.B. Romero, A. Ramizez, O.V. Galan, Sol. Energy **208**, 227 (2020)
36. B.H. Baby, D.B. Mohan, Appl. Surf. Sci. **423**, 1111 (2017)
37. M. Devika, K.T.R. Reddy, N.K. Reddy, K. Ramesh, R. Ganesan, E.S.R. Gopal, K.R. Gunasekhar, J. Appl. Phys. **100**, 023518 (2006)
38. M. Ichimura, K. Takeuchi, Y. Ono, E. Arai, Thin Solid Films **361**, 98–101 (2000)
39. J. Malaquias, P.A. Fernandes, P.M.P. Salome, A.F. da Cunha, Thin Solid Films **519**, 7416 (2011)
40. V.R.M. Reddy, S. Gedi, C. Park, R.W. Miles, K.T.R. Reddy, Curr. Appl. Phys. **15**, 588 (2015)
41. V. Robles, J.F. Trigo, C. Guillen, J. Herrero, Thin Solid Films **582**, 249 (2015)
42. T. Sall, M. Mollar, B. Marı, J. Mater Sci. **51**, 7607 (2016)
43. Z. Xu, Y. Chen, Energy Procedia **10**, 238 (2011)
44. M.R. Pallavolu, V.R.M. Reddy, P.R. Guddeti, C. Park, J. Mater. Sci.: Mater. Electron. **30**, 15980 (2019)
45. B.D. Cullity, S.R. Stock, *Elements of X-Ray Diffraction*, 3rd edn. (Prentice-Hall, Upper Saddle River, NJ, 2001)
46. T. Prasada Rao, M.C. Santhoshkumar, Appl. Surf. Sci. **255**, 4579 (2009)
47. Y.P.V. Subbaiah, P. Prathap, K.T.R. Reddy, Appl. Surf. Sci. **253**, 2409 (2006)
48. J. Tauc, R. Grigorovici, A. Vancu, Phys. Status Solidi B **15**, 627 (1966)
49. H. Wei, Z. Ye, M. Li, Y. Su, Z. Yang, Y. Zhang, CrystEngComm **13**, 2222 (2011)
50. M. Bar, W. Bohne, J. Rohrich, E. Strub, S. Lindner, M.C. Lux-Steiner, C.H. Fischer, T.P. Niesen, F. Karg, J. Appl. Phys. **96**, 3857 (2004)
51. A. Banotra, N. Padha, Sol. Energy **211**, 810–821 (2020)
52. A. Banotra, N. Padha, AIP Conf. Proc. **1942**, 080050 (2018)
53. A. Banotra, N. Padha, S. Kumar, A.K. Kapoor, AIP Conf. Proc. **1953**, 100050 (2018)

© The Author(s), under exclusive licence to The Materials Research Society 2021